Research Square

Preprints are preliminary reports that have not undergone peer review.
They should not be considered conclusive, used to inform clinical practice,
or referenced by the media as validated information.

Controlling the dynamics of electric field driven droplet on a lubricant-infused surface

Kai Luo

K.Luo@ucl.ac.uk

University College London https://orcid.org/0000-0003-4023-7259

Geng Wang

University College London

Junyu Yang

Timan Lei

Jin Chen

Halim Kusumaatmaja

University of Edinburgh https://orcid.org/0000-0002-3392-9479

Kai Li

https://orcid.org/0000-0002-3943-4602

Article

Keywords: electrohydrodynamics, droplet dynamics, lubricant infused surface

Posted Date: May 12th, 2026

DOI: https://doi.org/10.21203/rs.3.rs-9440505/v1

License: This work is licensed under a Creative Commons Attribution 4.0 International License.
Read Full License

Additional Declarations: There is **NO** Competing Interest.

Controlling the dynamics of electric field driven droplet on a lubricant-infused surface

Geng Wang[1,2,3], Junyu Yang[4], Timan Lei[5], Jin Chen[2], Halim Kusumaatmaja[4*], Kai Li[6,1,3*], Kai H. Luo[2*]

1. National Microgravity Laboratory, Institute of Mechanics, Chinese Academy of Sciences, Beijing 100190, China
2. Department of Mechanical Engineering, University College London, Torrington Place, London WC1E 7JE, UK
3. School of Engineering Science, University of Chinese Academy of Sciences, Beijing 100049, China
4. Institute for Multiscale Thermofluids, School of Engineering, The University of Edinburgh, Edinburgh, UK
5. Chair of Building Physics, Department of Mechanical and Process Engineering, ETH Zürich (Swiss Federal Institute of Technology in Zürich), Zürich 8092, Switzerland
6. School of Fundamental Physics and Mathematical Sciences, Hangzhou Institute for Advanced Study, UCAS, Hangzhou, 310024, China

* Corresponding Authors:
halim.kusumaatmaja@ed.ac.uk (H. K.)
likai@imech.ac.cn (K. L.)
k.luo@ucl.ac.uk (K. H. L.)

Summary

As a non-contact control approach, electric field (EF) can be utilised to drive droplet dynamics on a lubricant-infused surface (LIS), with numerous potential applications ranging from drug manufacturing to 3D printing. However, the resulting droplet dynamics remain poorly understood, especially as there are several possible droplet lubrication states on LIS. Here, we develop a lattice Boltzmann scheme that fully captures the interplay between the interfacial flows and electrohydrodynamics and harness it to investigate EF driven droplets on LIS. Combining simulations and analytical calculations, we establish quantitative expressions for the drag force and the electric force acting on a moving droplet. We demonstrate that the models can accurately capture droplet dynamics during programmable manipulation, including periodic motion and long-distance transport. Such reliable theoretical models can potentially transform precision control of droplet dynamics by removing the reliance on trial and error tests.

Keywords: electrohydrodynamics, droplet dynamics, lubricant infused surface.

Introduction

Non-contact manipulation of droplets is critical in a broad range of engineering applications, including digital microfluidics [1,2], chemical reactions [3,4], high-resolution printing [5], and water harvesting [6,7]. In general, droplet manipulation can be classified into two categories. Passive manipulation is achieved by designing geometric, chemical, or wettability-gradient surfaces that drive spontaneous motion towards a lower-energy state [8,9],

whereas active manipulation relies on external physical fields such as optical [10], acoustic [11], or electric fields [12,13]. Among these strategies, electric field (EF) based "electric tweezers" (ET) have attracted increasing attention in recent years [14,15]. Compared with other approaches, ET can be applied to most dielectric and leaky-dielectric liquids and requires no additional additives.

The fundamental principle of ET is based on electrohydrodynamics (EHD), where droplet motion results from a balance between electrostatic driving forces and resistive drag. Early ET approaches relied on superhydrophobic surfaces to minimise pinning [12,14,15]. However, control failure can occur when the applied electric field is too strong for a given droplet size [15,16], such that the upward electric force exceeds the surface pinning force, causing the droplet to lift off from the substrate rather than remain in lateral motion. More recently, an ET approach on lubricant-infused surfaces (LIS) has been proposed, thereby removing the reliance on superhydrophobic substrates [17,18]. The presence of the lubricant results in strong suppression of droplet's contact line pinning and contact angle hysteresis, resulting in highly mobile droplet motion. This strategy significantly broadens the applications of ET, enabling contactless, flexible, and robust droplet manipulation across a wide range of droplet sizes, compositions, and working conditions [17]. However, introducing a lubricant layer substantially increases the complexity of manipulation, as both the electric driving force and the drag force are closely related to the fluid properties, droplet position, and droplet velocity [19,20]. In most practical electric-tweezing applications, droplet manipulation still requires real-time observation of the droplet position to determine electrode actuation [15,17], which is cumbersome and unpractical for many applications.

To enable programmable droplet manipulation, theoretical models capable of accurately describing droplet dynamics under different operating conditions is urgently needed [16,21]. However, two major challenges remain. First, existing expressions for the drag force acting on droplets on LIS are still incomplete, particularly across different lubricant viscosities and surface wettabilities [19]. Primarily, this is because the droplet can exist in different lubrication states. Second, a temporally and spatially resolved description of the electric force acting on a droplet remains unavailable [21]. As a complement to experiments, numerical simulations provide an opportunity to investigate droplet dynamics on LIS over a wide range of operating conditions. Such numerical simulations are challenging as they must capture complex solid boundaries, three fluid phases (droplet, lubricant, and air), electrohydrodynamics (EHD), and their complex interplay. To the best of the authors' knowledge, a numerical approach capable of simulating EHD-coupled droplet dynamics on LIS is not previously available.

In this work, to overcome this challenge, we develop an EHD ternary multiphase LBM method. This is made possible by bringing together our recently proposed two-phase EHD LBM model for dielectric fluids [22] and multi-component LBM models for droplets on LIS [23,24]. Based on the proposed numerical model, we simulate EF driven liquid droplets on LIS. We first explore the forces acting on the droplet under different operating conditions and use the simulation insights to develop and validate theoretical models for the drag force and the electric force. We show that the resulting models can accurately describe programmable droplet manipulation using pre-designed electrode actuation protocols, including periodic droplet motion and long-distance transport.

Results

Figure 1 shows the physical problem considered in this study, a water droplet is deposited on a silicone oil infused micropillar surface and actuated by an electric field generated by an electrode positioned above the substrate near the upper-right corner of the domain. The substrate consists of rectangular micropillars of width $w_{\mathrm{p}} = 42.9\mu\mathrm{m}$, height $h_{\mathrm{p}} = 143.0\ \mu\mathrm{m}$, and edge to edge spacing $s_{\mathrm{p}} = 42.9\ \mu\mathrm{m}$, giving a solid fraction of $\phi = w_p^2/(w_p + s_p)^2 = 0.25$. Unless otherwise specified, the substrate is initially covered by a silicone oil layer with a thickness of $h_{\mathrm{oil}} = h_p$.The water–air, oil–water, and oil–air interfacial tensions are $\gamma_{\mathrm{wa}} = 72.5\ \mathrm{mN/m}$, $\gamma_{\mathrm{ow}} = 19.8\ \mathrm{mN/m}$, and $\gamma_{\mathrm{oa}} = 43.0\ \mathrm{mN/m}$, respectively. The remaining fluid properties are summarised in Table 1. It should be noted that, consistent with the experiments [17], a relatively low-viscosity silicone oil (< 10 cP) was selected as the lubricant, as a highly viscous lubricant would lead to extremely slow droplet motion when the droplet moves away from the electrode. On a flat solid surface, the intrinsic contact angles of water and oil are denoted by $\theta_{ws}$and θ_{os}, respectively. The electrode configuration is characterised by the electrode-surface distance h_e, electrode height l_e, and the horizontal separation S_e between the electrode and the droplet.

Table 1 Fluid properties used in the current study

	Air	Water	Silicone oil
Density	$\rho_{\mathrm{g}} = 998.0\ \mathrm{kg/m^3}$	$\rho_{\mathrm{w}} = 998.0\ \mathrm{kg/m^3}$	$\rho_{\mathrm{o}} = 970\ \mathrm{kg/m^3}$
Viscosity	$\mu_{\mathrm{g}} = 0.0179$ cP	$\mu_w = 1$ cP	$\mu_{\mathrm{o}} = 0.5\sim5$ cP
Electrical primitivity	$\varepsilon_{\mathrm{g}} = 8.9 \times 10^{-12}\ \mathrm{F/m}$	$\varepsilon_{\mathrm{w}} = 80\varepsilon_{\mathrm{g}}$	$\varepsilon_{\mathrm{o}} = 2.3\varepsilon_{\mathrm{g}}$
Electrical conductivity	$\sigma_{\mathrm{g}} = 1 \times 10^{-50}\ \mathrm{S/m}$	$\sigma_{\mathrm{w}} = 5 \times 10^{-6}\ \mathrm{S/m}$	$\sigma_0 = 1 \times 10^{-13}\ \mathrm{S/m}$

To realise this problem numerically, the simulations are performed in a three-dimensional computational domain of size $L_x \times L_y \times L_z = 7.2 \times 2.6 \times 2.2$ mm. In our simulation, the droplet initial volume is $\mathrm{Vol}_0 = 4\pi R_0^3/3 = 0.33 \sim 4.19\mu L$, corresponding to an effective radius of $R_0 = 0.43 \sim 1$ mm. The micropillar surface is prescribed as zero electric potential, the electrode is maintained at a fixed potential φ_0, and Neumann boundary conditions are imposed on all other walls. The characteristic electric-field strength is therefore defined as $E_0 = \varphi_0/L_y$. Unless otherwise stated, the spatial resolution is set to $\mathrm{d}x = R_0/35 = 14.3$ μm. A mesh-sensitivity assessment is provided in Supplementary Fig. 1.

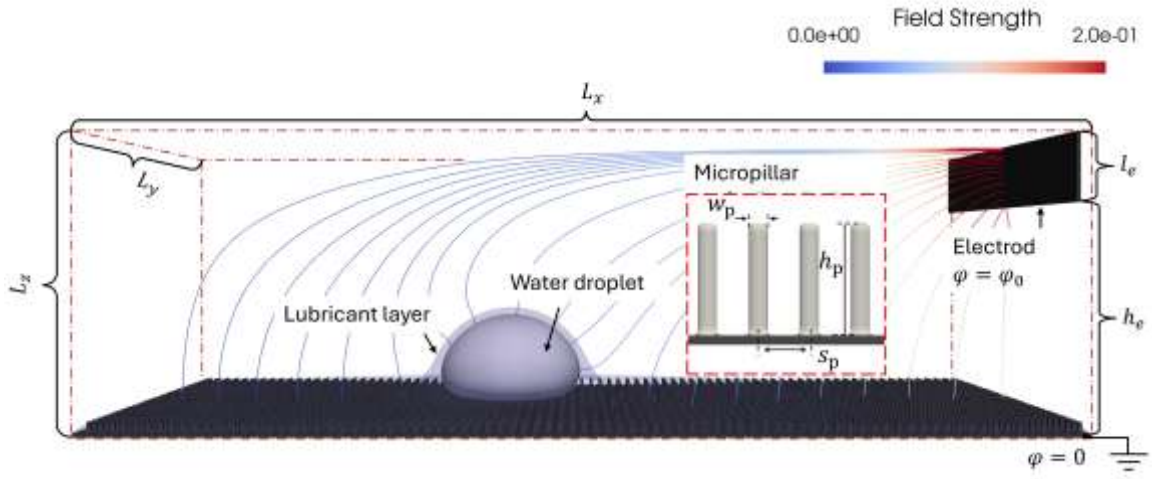


Figure 1. Schematic of computational domain.

Figure 2(a) presents typical simulation snapshots of droplet migration. In line with experiment observations [25–27], as the spreading coefficient of oil on water in the presence of air $I_{\mathrm{os(w)}} = \gamma_{\mathrm{wa}} - \gamma_{\mathrm{ow}} - \gamma_{\mathrm{oa}} > 0$, the droplet is fully cloaked by the lubricant oil. The droplet starts to migrate directionally (in the electrode direction) under the electric driving force. The droplet migration velocity (V) is primarily determined by the competition between the electric force (F_{ele}) and drag force (F_{drag}) [17]. For droplets moving on LIS, the drag force is dominated by viscous stresses [20]. In the upper panel of Fig. 2(b), we visualise the viscous dissipation of the liquid phases during droplet motion. As $\mu_{\mathrm{o}} < \mu_{\mathrm{w}}$, it can be observed that the dissipation is not only concentrated within the lubricant–droplet meniscus but also occurs inside the droplet (within the black contour), particularly near the micropillar contact region. The inset in the lower panel of Fig. 2(b) shows the charge distribution during droplet migration, where negative charges accumulate on the side facing the electrode due to electrostatic attraction. In addition, inspection of the electric field lines indicates that the field is primarily perturbed in the vicinity of the droplet, whereas it remains self-similar far from the droplet

during evolution. In this paper, we focus on the effects of the initial droplet–electrode distance (S_0), the electric field strength (E_0), the lubricant viscosity (μ_0) and the solid wettability (θ_{ws} and θ_{os}) on droplet motion. The first two parameters mainly determine F_{ele}, whereas the latter two parameters control the magnitude of F_{drag}. Consequently, the droplet exhibits distinct migration velocities under various combinations of these operating conditions, as illustrated in Fig. 2(c).

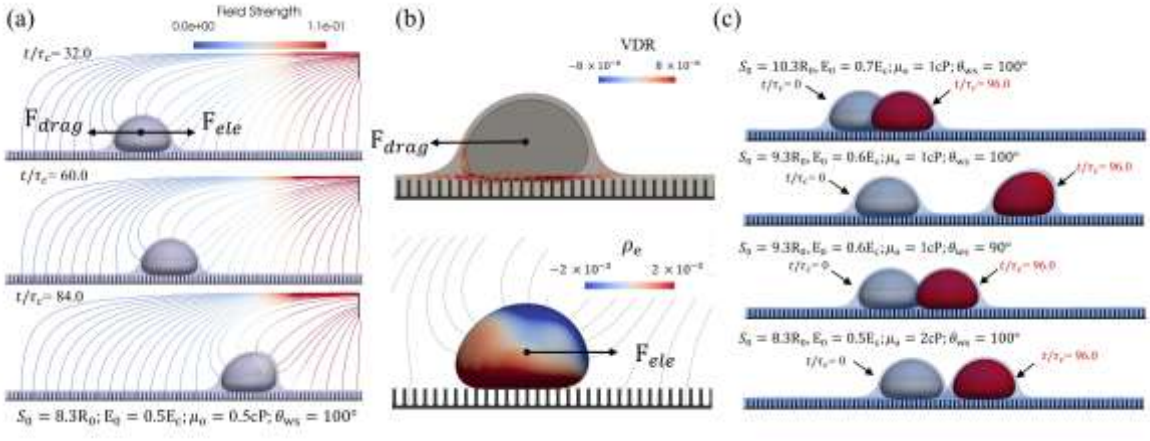


Figure 2. Droplet dynamics under different operating conditions: (a) Droplet migration for the case with $S_0 = 8.3R_0$, $E_0 = 0.5E_{\mathrm{c}}$, $\mu_{\mathrm{o}} = 0.5$ cP, $\theta_{\mathrm{os}} = 5°$ and $\theta_{\mathrm{ws}} = 100°$. The lines in the figures denote electric field lines. (b) Viscous dissipation (upper panel) and charge density distribution of the moving droplet. (c) Initial (white colour) and terminal (red colour) droplet positions at $t/\tau_{\mathrm{c}} = 96.0$ for different combinations of S_0, E_0, μ_{o} and θ_{ws}.

The first issue to be discussed is the drag force (F_{drag}) experienced by a droplet moving on LIS. In recent years, F_{drag} for lubricant dissipation dominated regime has been extensively studied [20,28]. In this regime, F_{drag} increases with the capillary number ($\mathrm{Ca} = \mu_{\mathrm{o}}V/\gamma_{\mathrm{ow}}$) following an approximate $F_{\mathrm{drag}} \propto \mathrm{Ca}^{2/3}$ scaling [29,30]. This behaviour is attributed to viscous dissipation being primarily localised within the Landau-Levich-Derjaguin (LLD) film [31,32], with thickness can be scaled as $h_{\mathrm{LLD}} \sim R_0\mathrm{Ca}^{2/3}$. The lubricant dissipation dominated regime is typically observed when $h_{\mathrm{LLD}} > h_{\mathrm{p}}$ and $\mu_{\mathrm{o}} \gg \mu_{\mathrm{w}}$, and the $F_{\mathrm{drag}} \propto \mathrm{Ca}^{2/3}$ scaling is captured by our model, as shown in the Model validations section. In this paper, as discussed above, our cases correspond to the droplet dissipation dominated regime (i.e., for $h_{\mathrm{LLD}} \ll h_{\mathrm{p}}$ and $\mu_{\mathrm{o}}/\mu_{\mathrm{w}} < 10$). Previous studies [23,31,33] pointed out that F_{drag} follows a linear dependence on Ca in this regime. To verify this scaling, we simulate a droplet deceleration during sliding on a lubricant-infused pillar surface with an initial velocity V_0. We test six cases with different V_0, Vol_0 and compute F_{drag} by $F_{\mathrm{drag}} = -mdV/dt$ ($m = \rho_{\mathrm{w}}\mathrm{Vol}_0$ is droplet mass). The corresponding evolutions of droplet displacement, S, and velocity, V, can

be found in Supplementary Fig. S2. As shown in Fig. 3(a), the calculated drag force F_{drag} agrees well with both the theoretical prediction $F_{\mathrm{drag}}/(2\gamma_{ow}R_0) = 3.5\pi(R_0/h_p)^{0.5}\mathrm{Ca}$ and the experimental data reported in Ref. [31] (solid line and red symbols in Fig. 3(a)). Present simulation data in Fig. 3(a) gives a slightly smaller best-fit perfector of 3.3 (dashed line in Fig.3(a)), compared with the experimental value of 3.5.

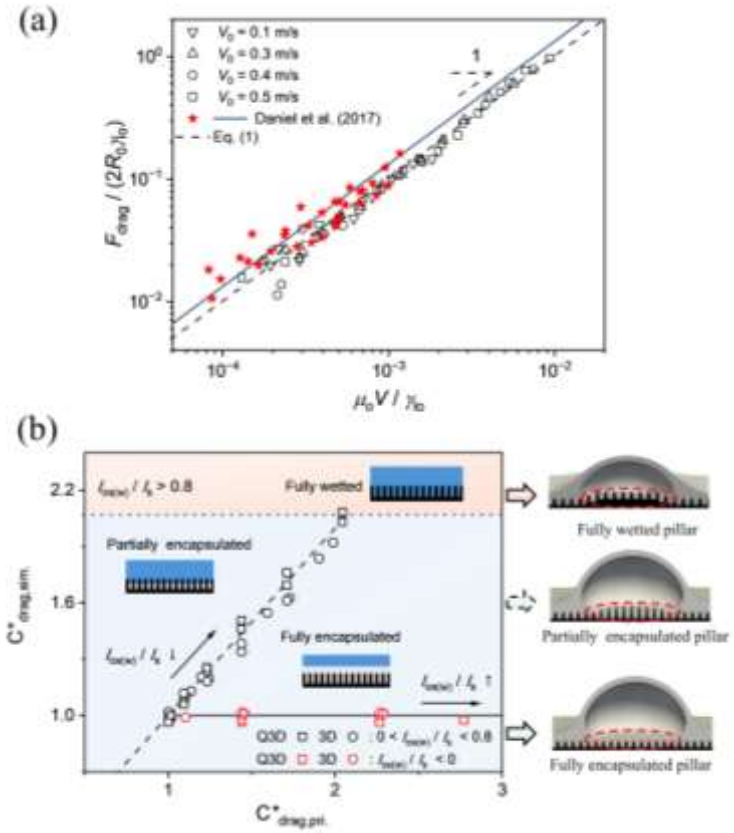


Figure 3. (a) The normalized drag force $F_{\mathrm{drag}}/(2\gamma_{ow}R_0)$ as a function of $\mu_o V/\gamma_{lo}$ during droplet motion, where the red symbols and dashed line denote the experimental data and theoretical equation in Ref. [31]. (b) Comparison between the dimensionless drag coefficient predicted by the proposed theoretical model ($C^*_{\mathrm{drag,pri}}$) and LBM simulations ($C^*_{\mathrm{drag,sim}}$). The red shaded region corresponds to $I_{\mathrm{os(w)}}/I_s > 0.8$. In the blue-shaded region, the dashed and solid lines denote $C^*_{\mathrm{drag,sim}} = C^*_{\mathrm{drag,pri}}$ and $C^*_{\mathrm{drag,pri}} = 1$, respectively. In the inset of panel (b), the grey, blue, and black regions represent the lubricant oil, the droplet, and the micropillars, respectively.

In this paper, we further extend the model of F_{drag} to a broader range of liquid viscosities and pillar wettabilities, which has not been systemically explored before. For lubricant dissipation dominated cases, F_{drag} is assumed to scale linearly with μ_{o} [28]. However, when dissipation within the droplet is non-negligible, the viscosity of droplet must be taken into account. Here, we replace μ_o in the original model with an effective viscosity $\bar{\mu} = \left(\mu_{\mathrm{o}}\mu_{\mathrm{w}}\mu_{\mathrm{g}}\right)^{1/3}$ defined by the geometric mean of ternary system. In addition, we introduce an

interfacial tension factor $I_{\mathrm{os(w)}}/I_{\mathrm{s}}$ to incorporate the effect of pillar wettability. Inspired by Ref. [26], by substituting water-solid interfacial tension $\gamma_{\mathrm{sw}} = \gamma_{\mathrm{sg}} - \gamma_{\mathrm{wg}}\cos(\theta_{\mathrm{ws}})$ and oil-solid interfacial tension $\gamma_{\mathrm{os}} = \gamma_{\mathrm{sg}} - \gamma_{\mathrm{og}}\cos(\theta_{\mathrm{os}})$ to Young's equation $\cos\left(\theta_{\mathrm{os(w)}}\right) = (\gamma_{\mathrm{sw}} - \gamma_{\mathrm{so}})/\gamma_{\mathrm{ow}}$, the spreading coefficient of oil on the pillar surface in the presence of water can be defined as $I_{\mathrm{os(w)}} = \gamma_{\mathrm{og}}\cos(\theta_{\mathrm{os}}) - \gamma_{\mathrm{wg}}\cos(\theta_{\mathrm{ws}}) - \gamma_{\mathrm{ow}}$. Theoretically, when $I_{\mathrm{os(w)}} > 0$, the contact angle of oil on the pillar surface in the presence of water is 0°, which implies the oil completely wets the pillar surface and the pillar surface exhibits fully encapsulated (see the fully encapsulated schematic in the inset of Fig. 3(b)). Next, introducing $I_{\mathrm{s}} = -\gamma_{\mathrm{ow}}$ as reference quantity associated with the oil-water interfacial tension, when $I_{\mathrm{os(w)}} < I_{\mathrm{s}}$, the spreading of water overcomes the interfacial tension of the oil–water layer, such that water fully displaces the oil from the pillar surface (see the fully wetted schematic in the inset of Fig. 3(b)). Finally, for $0 < I_{\mathrm{os(w)}}/I_{\mathrm{s}} < 1$, the droplet penetrates into the pillar array, leading to partial exposure of the pillar tops, and $I_{\mathrm{os(w)}}/I_{\mathrm{s}}$ quantifies the extent of water penetration into the pillar gaps. A new expression for F_{drag} which accounts for viscosity effects and pillar wettability can be obtained by introducing an empirical fitting coefficient C_{drag}.

$$F^*_{\mathrm{drag}} = \frac{F_{\mathrm{drag}}}{2\gamma_{\mathrm{ow}}R_0} = 3.5\pi C_{\mathrm{drag}}(R_0/h_p)^{0.5}\mathrm{Ca}, \tag{1a}$$

$$C_{\mathrm{drag}} = C_\alpha\left(1 + 1.5\left(\frac{I_{\mathrm{os(w)}}}{I_{\mathrm{s}}}\right)^2\right)\frac{\bar{\mu}}{\mu_0}. \tag{1b}$$

Where C_α is a fitting constant which value depends on the simulation configuration (3D or Q3D) and the initial lubricant thickness h_{oil}. In the 3D simulations, $C_\alpha = 18.2$ for $h_{\mathrm{oil}} = h_p$ and $C_\alpha = 16.4$ for $h_{\mathrm{oil}} = 1.2h_p$. In the Q3D simulations, the corresponding values are $C_\alpha = 6.8$ and $C_\alpha = 6.1$, respectively, the corresponding correlation analysis is provided in the Supplementary Material. To validate the model for F_{drag} in Eq. (1), we carry out simulations to different θ_{ws}, θ_{os} and μ_o. Considering that the lubricant oil is usually highly wetting on the solid surface for LIS, we restrict our simulations to $\theta_{os} \leq 40°$. Similar to Fig. 3(a), we simulate a droplet deceleration and obtain S from solving deceleration equation of moving droplet $\mathrm{d}^2S/\mathrm{d}t^2 = -F_{\mathrm{drag}}/m$. The comparisons between the theoretical displacement and the numerical results are provided in Supplementary Fig. S3, showing that the proposed model accurately captures the droplet dynamics over a wide range of viscosities and surface wettabilities.

To further assess the generality of the proposed drag model, we perform full 3D and Q3D simulations and compare the simulated drag coefficient, $C_{\mathrm{drag,sim}} = mV_0/(2R_0\bar{\mu}S_{max})$ (S_{max} is the maximum displacement of droplet) with the theoretical prediction $C_{\mathrm{drag,pri}}$ in Eq. (1). A comparison between the normalised $C^*_{\mathrm{drag,sim}}$ and $C^*_{\mathrm{drag,pri}}$ is shown in Fig. 3(b), with both coefficients normalised by $C_{\mathrm{drag}}(I_{\mathrm{os(w)}}/I_{\mathrm{s}} = 0)$. Figure 3(b) reveals three distinct regimes. First, when $I_{\mathrm{os(w)}}/I_{\mathrm{s}} > 0.8$, the lubricant film beneath the droplet is completely depleted and the droplet becomes pinned on the micropillars, as illustrated by the inset in the red-shaded region. This critical value is slightly lower than the theoretical threshold $I_{\mathrm{os(w)}}/I_{\mathrm{s}} > 1$. We suspect that this discrepancy may arise from numerical artefacts associated with the diffuse-interface model used in this study. Second, when $0 < I_{\mathrm{os(w)}}/I_{\mathrm{s}} < 0.8$, $C^*_{\mathrm{drag,sim}}$ agrees well with $C^*_{\mathrm{drag,pri}}$ and increases as $I_{\mathrm{os(w)}}/I_{\mathrm{s}}$ decreases. In this regime, the droplet partially penetrates into the micropillars, as shown in the inset of Fig. 3(b), which is the main reason for the increased drag. Finally, when $I_{\mathrm{os(w)}}/I_{\mathrm{s}} < 0$, the lubricant film beneath the droplet remains continuous and prevents direct contact between the droplet and the micropillars. The droplet therefore slides entirely on the lubricant layer, and the drag coefficient approaches an approximately constant value, close to $C_{\mathrm{drag}}(I_{\mathrm{os(w)}}/I_{\mathrm{s}} = 0)$.

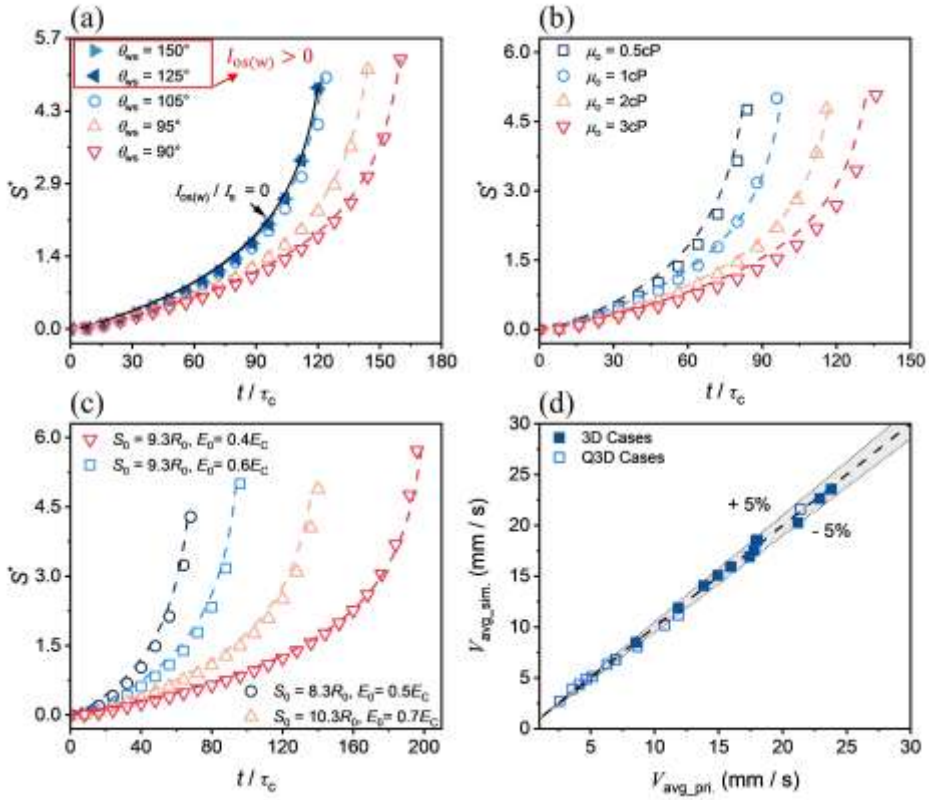


Figure 4. Transient evolution of an electric field driven droplet by varying different operating conditions:(a) droplet–solid apparent contact angle θ_{ws}; (b) lubricant viscosity μ_{o}; (c) initial droplet–electrode distance S_0 and

electric field strength E_0, where symbols denote LBM simulation results, lines represent predictions from the theoretical model. Figure (d) is a comparison of the droplet average velocity obtained from LBM simulations and theoretical predictions.

The results in Fig. 3(b) reveal two important mechanisms: (1) The drag force acting on a droplet on LIS can be tuned by adjusting surface wettability, such as θ_{os} and θ_{ws}; (2) When $I_{\mathrm{os(w)}}/I_{\mathrm{s}} < 0$, the drag force becomes independent of surface wettability. This regime can be accessed by varying the droplet, lubricant, and/or solid such that contact angles satisfy the inequality $\gamma_{\mathrm{og}}\cos(\theta_{\mathrm{os}}) - \gamma_{\mathrm{wg}}\cos(\theta_{\mathrm{ws}}) - \gamma_{\mathrm{ow}} < 0$. It should be noted that, consistent with the previous findings [34], we observe that within the present regime of relatively sparse solid fraction ($\phi < 0.25$) and sufficiently tall micropillars ($h_{\mathrm{LLD}} \ll h_p$), variations in pillar height and interpillar spacing do not lead to a noticeable change in C_{drag}. A detailed sensitivity analysis is provided in the Methods section.

We next discuss the electric force acting on the droplet during migration. When the droplet is sufficiently small compared with the computational domain, the electric force can be approximated using a point-dipole dielectrophoretic (DEP) model [35,36]. Besides, since $\varepsilon_w \gg \varepsilon_o$ and $\sigma_w \gg \sigma_o$, the Coulomb and polarisation forces acting on the lubricant film are negligible compared with those acting on the droplet. For a DC electric field, the time-averaged DEP force on a dielectric sphere can be written as:

$$\begin{cases} F_{\mathrm{ele}} \sim K_e \dfrac{d(|\boldsymbol{E}|_x^2)}{dx}, \\ K_e = 2\pi\varepsilon_{\mathrm{w}} R_0^3 \dfrac{\sigma_{\mathrm{w}} - \sigma_o}{\sigma_{\mathrm{w}} - 2\sigma_o}, \end{cases} \tag{2}$$

where $\nabla(|\boldsymbol{E}|_x^2)$ is the gradient of the squared electric field magnitude along the direction of motion. As shown in Fig. 2(a), the droplet perturbs the electric field mainly in the vicinity of the interface. In the far field, the electric potential still satisfies Laplace's equation $\nabla^2\varphi = 0$, solving Laplace's equation yields:

$$F_{\mathrm{ele}} = K_e C_{\mathrm{ele}} e^{-2\alpha_0 S_e}, \tag{3}$$

with:

$$\begin{cases} C_{\mathrm{ele}} = \dfrac{2\alpha_0\varphi_0^2\, cos^2(\alpha_0 l_e)}{\left(J_D(\alpha_0) + \alpha_0 J_N(\alpha_0)\right)^2}, \\ \alpha_0 = \dfrac{\pi}{2(h_e + l_e)}, \qquad J_N(\alpha_0) = \dfrac{l_e}{2} - \dfrac{sin(2\alpha_0 l_e)}{4\alpha_0}, \qquad J_D(\alpha_0) = \dfrac{h_e}{2} + \dfrac{sin(2\alpha_0 l_e)}{4\alpha_0}. \end{cases} \tag{4}$$

A detailed derivation of the above analytical solution is provided in the Supplementary Material, together with a comparison with the LBM simulation results presented in

Supplementary Fig. S4. When the initial droplet–electrode distance is S_0, combining F_{drag} with F_{ele}, the equation of motion for an EF driven droplet on LIS can be written as:

$$m\frac{d^2S}{dt^2} = C_{\mathrm{drag}} \cdot 2R_0\bar{\mu}\frac{dS}{dt} + \Lambda K_e C_{\mathrm{ele}} e^{-2\alpha_0(S_0-S)}, \tag{5}$$

where Λ is a free parameter that balances the relative contributions of the drag force and the electric driving force. We find $\Lambda_{3\mathrm{D}} \approx 0.012$ for 3D cases. With the initial conditions $S(0) = 0$ and $V_0 = 0$, the evolution of droplet displacement can be solved for different operating conditions.

Figures 4(a-c) show the time evolution of the dimensionless droplet displacement ($S^* = S/R_0$) under different θ_{ws}, $\bar{\mu}$, S_0 and E_0. Our proposed theoretical model agrees well with the simulation results. Moreover, consistent with the analysis in Fig. 3(b), for cases with $I_{\mathrm{os(w)}}/I_{\mathrm{s}} < 0$, varying the droplet and lubricant wettability have a negligible influence on the droplet migration. To achieve active control of droplet migration, a key requirement is to predict the relationship between migration distance and droplet travel time under various operating conditions [18]. When the droplet is far from the electrode, the viscous relaxation time $\tau_v \sim m/(2C_{\mathrm{drag}}R_0\bar{\mu})$ is much smaller than the electric force varies timescale. Equation (5) therefore admits the approximate analytical form:

$$\frac{dt}{dS} \approx \frac{2C_{\mathrm{drag}}R_0\bar{\mu}}{\Lambda_1 K_e C_{ele} e^{-2\alpha_0(S_0-S)}} + \frac{\alpha_0 m}{C_{\mathrm{drag}}R_0\bar{\mu}}. \tag{6}$$

Integrating Eq. (6) from S_0 to S_t, the total transport time for a droplet moving can be estimated as:

$$t_{S_0\sim S_t} = \frac{R_0\bar{\mu}C_{\mathrm{drag}}}{\alpha_0\Lambda_1 K_e C_{ele}}\left(e^{2\alpha_0 S_0} - e^{2\alpha_0(S_0-S_t)}\right) + \left(\frac{\alpha_0 m}{R_0\bar{\mu}C_{\mathrm{drag}}}\right)S_t. \tag{7}$$

Figure. 4(d) shows a comparison between the theoretically predicted and simulated average velocities $V_{avg} = (S_0 - S_t)/t_{s_0\sim s_t}$ for droplet travel distance $S_0 - S_t = 3R_0$. The maximum error of the theoretical prediction (Eq. 7) does not exceed 7% for all cases. We further performed Q3D simulations to assess the generality of the droplet transport model. The theoretical prediction remains valid for the Q3D cases, the only difference is that the fitting parameter $\Lambda_{1,\mathrm{Q3D}} = \Lambda_{1,3\mathrm{D}}/2$.

Building on our theoretical model, we enable active control by pre-designing electrode switching protocols for different transport modes. In this work, we propose two electrode-control strategies to realise periodic and long-distance droplet transport. First, we place a droplet in the middle of two electrodes and control its motion by setting the switching times of

electrodes e_1 and e_2. We initially activate e_1 to drive the droplet. When the droplet approaches electrode e_1 such that the droplet–electrode distance S_{e1} decreases to $4.5R_0$, we switch off e_1 and activate e_2. When the droplet subsequently moves back and the droplet–electrode distance to e_2, denoted by S_{e2}, decreases to $4.5R_0$, we switch off e_2 and reactivate e_1. The switching times are obtained by solving Eqs. (5) and (7). A transient snapshot of the bidirectional droplet motion is shown in Fig. 5(a), respectively, together with the corresponding quantitative evaluation of droplet displacement. In addition, the animation of the bidirectional droplet is shown in Supplementary Movie 1. Our LBM simulations confirm that periodic droplet motion can be achieved through electrode switching, and the simulated displacement agrees closely with the theoretical prediction. It is worth noting that a small deviation in the switching time can significantly alter the droplet migrate. As an illustration, we plot the theoretical displacement curves obtained when the first switching time (t_{sw1}) is advanced by 10% or delayed by 10%. The corresponding time for the droplet to reach the second switching point (t_{sw2}) differs by approximately 50%. This sensitivity highlights that an accurate theoretical model is essential for achieving reliable active control of droplet transport.

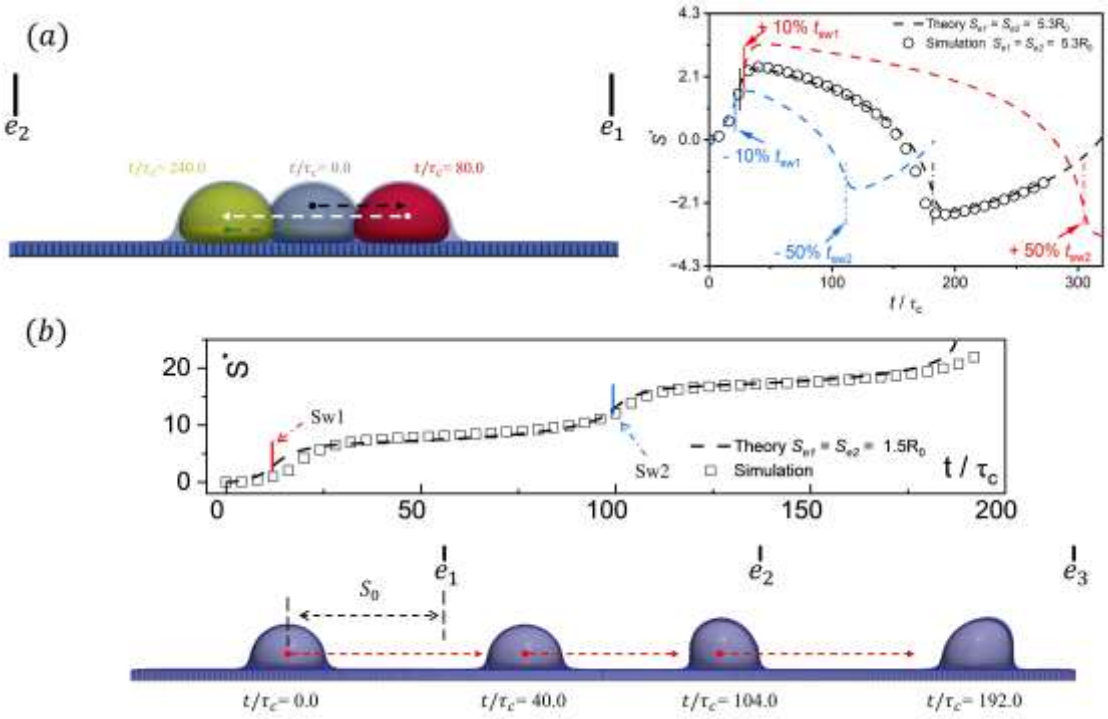


Figure 5. Simulation of directional droplet motion driven by an electric field. (a) Left: qualitative snapshots of periodic droplet motion, with different colour correspond to different time instants. Right: quantitative comparison between the simulated droplet displacement and the theoretical prediction. (b) Top: quantitative comparison between the simulated droplet displacement and the theoretical prediction for long-distance droplet transport. Bottom figure corresponding qualitative snapshots.

Finally, similar to the experiment in Ref. [15] ,we simulate long-distance droplet transport driven by multiple electrodes. We consider three electrodes separated by a fixed spacing S_e, with the initial droplet–electrode distance set to $S_0 = 5R_0$. The electrodes are switched when the droplet approaches the active electrode to $S_{e1} = S_{e2} = 1.5R_0$. Considering the substantial computational cost of this simulation, we adopted a thicker initial lubricant layer ($h_{\mathrm{oil}} = 1.2h_p$) in this case to reduce F_{drag} (as discussed in Supplementary Material), thereby shortening the simulation time. The animation of the long-distance droplet transport is shown in Supplementary Movie 2. Similar to case in figure 5(a), the switching times are obtained by solving Eqs. (5) and (7). Figure 5(b) presents the quantitative evolution of the droplet displacement together with representative snapshots. It can be found that the theoretical model accurately predicts the droplet displacement for this long-distance droplet transport problem. A small deviation can be observed between the theoretical model and the simulation results at the initial stage ($t/\tau_{\mathrm{c}} < 25$) and final stage ($t/\tau_{\mathrm{c}} > 25$). This discrepancy arises from a limitation of the point-dipole dielectrophoretic model used to evaluate the electric force, which is derived under the assumption of an infinite domain. In the present case, the electrode is initially located close to the droplet and the electrode still active at final stage, so finite size effects of the droplet are no longer negligible. As a result, the point-dipole approximation becomes less accurate, leading to the observed deviation.

Conclusion

In this work, we conducted a systematic investigation into the dynamics of EF-driven droplets on LIS and revealed the competition of forces governing droplet motion under different operating conditions. Our results show that the lubrication state and the drag force of a droplet on LIS can be tuned by modifying the surface wettability of the solid substrate. The interfacial tension factor $I_{\mathrm{os(w)}}/I_{\mathrm{s}}$ can be used to characterise the droplet lubrication state on LIS. In addition, through rigorous mathematical derivation, we proposed a temporally and spatially resolved description of the electric force acting on a droplet during migration. By combining the electric driving force with the drag-force model, we established a theoretical equation to predict droplet motion under different operating conditions. Based on the proposed theoretical model, we designed programmable droplet manipulation by pre-setting the electrode-switching times and electrode arrangement, enabling periodic droplet motion and long-distance droplet transport.

One important outcome of this study is the establishment of the quantitative relationship between drag force and surface wettability, providing new insight for the precise control of droplet dynamics on LIS. In addition, the proposed theoretical equation for EF-driven droplets on LIS enables prediction of droplet motion across multiple operating parameters. Based on this theoretical framework, droplet motion becomes predictable once the physical properties of the droplet and lubricant, the wettability of the micropillar surface, and the electrode position and field strength are specified. This work overcomes the limitation in EF-driven droplet manipulation on LIS that requires continuous monitoring of droplet position to adjust the electrode configuration and opens up new avenues to droplet manipulation in applications such as 3D printing, printed electronics, microfluidics, and drug delivery.

Method

Governing equations for the ternary multiphase EHD model

Electric field driven droplets on LIS represent a typical ternary multiphase EHD problem. Before constructing the numerical model, several assumptions are specified. First, the three fluid phases are assumed to be incompressible and immiscible. Second, compressibility effects are neglected, and each phase is treated as a Newtonian fluid with constant properties. Third, the multiphase EHD flow is described using the leaky dielectric model (LDM) [37]. Surface charges are treated as volumetric charges distributed within the interfacial diffusion layer, and no free charges are assumed to exist in the bulk fluids.

In the present model, a phase-field approach is adopted to simulate the ternary multiphase flow, and an improved conservative Allen–Cahn (AC) equation is employed for interface tracking [38]:

$$\frac{\partial \Phi_i}{\partial t} + \nabla \cdot (\Phi_i \boldsymbol{u}) = M_i \nabla \cdot \left(\nabla \Phi_i - \frac{4\mathbf{n}_i}{W_{int}} |\Phi_i(1-\Phi_i)| + \frac{\Phi_i^2}{\sum \Phi_i^2} \sum \frac{4\mathbf{n}_i}{W_{int}} |\Phi_i(1-\Phi_i)| \right), \quad (8)$$

where $\mathbf{u} = [u_x, u_y, u_z]$is the fluid velocity. $\Phi_i (i = 1,2,3)$ denote the phase indicators of the ternary components and satisfy the constraint $\Phi_1 + \Phi_2 + \Phi_3 = 1$. The phase interfaces are identified by $\Phi_i = 0.5$.$\mathbf{n}_i = \nabla\Phi_i/|\nabla\Phi_i|$ is the unit normal vector to the interface of component i. M_i represents the mobility, and W_{int} denotes the interface thickness. In the present study, to ensure numerical stability and accuracy when simulating multicomponent flows with large density ratios, we set $M_1 = M_2 = M_3 = 0.0025$ and $W_{\mathrm{int}} = 5$.

In the phase field model, the conservative AC equation is coupled with incompressible NS equations for the fluid flow, where [39]:

$$\nabla \cdot \boldsymbol{u} = 0,$$

$$\frac{\partial(\rho \boldsymbol{u})}{\partial t} + \nabla \cdot (\rho \boldsymbol{u}\boldsymbol{u}) = -\nabla P + \nabla \cdot \left(\rho \nu (\nabla \boldsymbol{u} + \nabla \boldsymbol{u}^T) + \rho \left(\nu_b - \frac{2}{3}\nu\right)(\nabla \cdot \boldsymbol{u})\mathbf{I}\right) + \boldsymbol{F_s} + \boldsymbol{F_e}. \quad (9)$$

ρ denotes the fluid density, ν is the kinematic viscosity, ν_b represents the non-hydrodynamic bulk viscosity, and P is the pressure. For the ternary phase-field model, the surface tension force is given by $\boldsymbol{F_s} = \mu_{\Phi_i} \nabla \Phi_i$, and the ternary chemical potential is defined as [40]:

$$\mu_{\Phi_i} = \frac{24\Upsilon_i}{W_{int}} \Phi_i (\Phi_i - 1)(\Phi_i - 0.5) - \frac{24\Upsilon_T}{W_{int}} \Phi_1 \Phi_2 \Phi_3 - \frac{3}{4}\Upsilon_i W_{int} \nabla^2 \Phi_i, \quad (10)$$

Υ_T and Υ_i are parameters related to the surface tension:

$$\begin{aligned} 3\Upsilon_T^{-1} &= \Upsilon_1^{-1} + \Upsilon_2^{-1} + \Upsilon_3^{-1}, \\ \Upsilon_1 &= \gamma_{12} + \gamma_{13} - \gamma_{23}, \\ \Upsilon_2 &= \gamma_{12} + \gamma_{23} - \gamma_{13}, \\ \Upsilon_3 &= \gamma_{13} + \gamma_{23} - \gamma_{12}. \end{aligned} \quad (11)$$

The above ternary multiphase model is coupled with the LDM model for EHD problem. In LDM, the electric force ($\boldsymbol{F_e}$) can be expressed as [37]:

$$\boldsymbol{F_e} = \rho_e \mathbf{E} - \frac{1}{2}\mathbf{E}^2 \nabla \varepsilon, \quad (12)$$

where $\mathbf{E} = -\nabla \varphi$ is electric field strength. φ stands for the electric potential, ε is dielectric permittivity, ρ_e is electrical charge density and fluid density. The governing equation of the electric field follows Gauss's law:

$$\nabla \cdot (\varepsilon \nabla \varphi) = -\rho_e. \quad (13)$$

The charge conservation equation is used to describe the evolution of charge density [41,42], where:

$$\frac{\partial \rho_e}{\partial t} + \nabla \cdot (\rho_e \boldsymbol{u}) - \nabla \cdot (\sigma \nabla \psi) - \alpha \nabla^2 \rho_e = 0, \quad (14)$$

α is the charge diffusion number, and σ is the electrical conductivity of the fluid. The introduced leaky dielectric model (LDM) has been extensively adopted and validated in our recent studies [22,43]. It has demonstrated the capability to accurately reproduce a broad range of challenging EHD problems, including Rayleigh fission, electrospray, droplet equatorial streaming, and EF enhanced pool boiling.

Unified Lattice Boltzmann Model for the ternary multiphase EHD model

In this work, the Unified Lattice Boltzmann Model (ULBM) proposed by Luo et al. [44] is employed to solve the governing equations presented in the preceding sections. ULBM is a unified framework that incorporates different collision models, multiphase flow models, and force schemes. To recover the target AC equation, a D3Q17 multi-relaxation time (MRT) ULBM is constructed, the collision operator of ULBM in raw moment space can be written as:

$$\mathbf{m}_{\Phi_i}^{*} = \left(\mathbf{I} - \mathbf{S}_{\Phi_i}\right)\mathbf{m}_{\Phi_i} + \mathbf{S}_{\Phi_i}\mathbf{m}_{\Phi_i}^{\mathbf{eq}} + \Delta t\left(\mathbf{I} - \frac{\mathbf{S}_{\Phi_i}}{2}\right)\mathbf{M}C_{\Phi_i}, \tag{15}$$

where $\mathbf{m}^{*}$, $\mathbf{m}^{\boldsymbol{eq}}$ are post-collision distribution moment set and equilibrium moment set, respectively. $\mathbf{I}$ stands for the unit matrix and $\mathbf{S}$ is the relaxation matrix. The superscript Φ_i represents the phase indicator, $\boldsymbol{e}_n$ and $\Delta t = 1$ are the discrete velocities and the time step, respectively. In this study, the transformation matrix $\mathbf{M}$ is chosen as the simplified non-orthogonal moment set which was originally proposed by Fei et al. [45,46]. The equilibrium distribution function for component i can be as:

$$f_{\Phi_i,n}^{eq} = \Phi_i\omega(|\boldsymbol{e}_n|^2)\left[1 + \frac{\boldsymbol{e}_n.\boldsymbol{u}}{c_s^2}\right], \tag{16}$$

where the weighs are $\omega(0) = 1/3$, $\omega(1) = 1/18$, and $\omega(2) = 1/36$ for D3Q19 model, and $C_s = 1/\sqrt{3}$ stands for the lattice sound speed. Multiplying the transformation matrix $\mathbf{M}$, the raw moment space discrete equilibrium moment is $\mathbf{m}_{\Phi_i}^{\mathbf{eq}} = \mathbf{M}f_{\Phi_i,n}^{eq}$, the forcing term can be written as [47]:

$$C_{\Phi_i,n} = \frac{\omega(|\boldsymbol{e}_n|^2)}{c_s^2}\boldsymbol{e}_n\left(\boldsymbol{F}_{\Phi_i,n} + \frac{\partial(\Phi_i\boldsymbol{u})}{\partial t}\right), \tag{17}$$

$\boldsymbol{F}_{\Phi_i,n}$ is given by:

$$\boldsymbol{F}_{\Phi_i,n} = \left[F_{\Phi_i,x}, F_{\Phi_i,y}, F_{\Phi_i,z}\right] = \frac{4\mathbf{n}_i}{W_{int}}|\Phi_i(1-\Phi_i)| - \frac{\Phi_i^2}{\sum\Phi_i^2}\sum\frac{4\mathbf{n}_i}{W_{int}}|\Phi_i(1-\Phi_i)|, \tag{18}$$

and the phase indicators can be calculated by:

$$\Phi_i = \sum_n f_{\Phi_i,n}, \tag{19}$$

The distribution function for Φ_i ($f_{\Phi_i,n}$) is reconstructed by $f_{\Phi_i,n} = \mathbf{M}^{-1}\mathbf{m}_{\Phi_i}^{*}$ after the collision in the raw moment space. To model the wetting behaviours involved in the simulation, we employed an energy-based contact angle model, in which the relationship between the solid phase indicator ($\Phi_{i,s}$) and the apparent contact angle (θ) can be expressed as [48]:

$$\begin{aligned}
\boldsymbol{n}\cdot\nabla\Phi_{1,s} &= \frac{4}{W_{int}}\left(-\cos(\theta_{13})\Phi_{1,s}\Phi_{3,s} - \cos(\theta_{12})\Phi_{1,s}\Phi_{2,s}\right),\\
\boldsymbol{n}\cdot\nabla\Phi_{2,s} &= \frac{4}{W_{int}}\left(\cos(\theta_{12})\Phi_{1,s}\Phi_{2,s} - \cos(\theta_{23})\Phi_{2,s}\Phi_{3,s}\right),\\
\boldsymbol{n}\cdot\nabla\Phi_{3,s} &= \frac{4}{W_{int}}\left(\cos(\theta_{23})\Phi_{2,s}\Phi_{3,s} + \cos(\theta_{13})\Phi_{1,s}\Phi_{3,s}\right).
\end{aligned} \tag{20}$$

θ_{ij} stands for the contact angle of the interface shaped by fluid i and j with the solid surface.

The incompressible Navier–Stokes equations, the charge conservation equation, and the Poisson equation are solved using a methodology similar to that adopted in our recent studies [22,43]. For example, two different distribution functions are introduced:

$$\begin{aligned}\mathbf{m}_g^* &= (\mathbf{I}-\mathbf{S}_g)\mathbf{m}_g + \mathbf{S}_g\mathbf{m}_g^{eq} + \Delta t\left(\mathbf{I}-\frac{\mathbf{S}_g}{2}\right)\mathbf{R}_g,\\ \mathbf{m}_{\rho_e}^* &= (\mathbf{I}-\mathbf{S}_{\rho_e})\mathbf{m}_{\rho_e} + \mathbf{S}_{\rho_e}\mathbf{m}_{\rho_e}^{\mathrm{eq}} + \Delta t\left(\mathbf{I}-\frac{\mathbf{S}_{\rho_e}}{2}\right)\boldsymbol{R}_{\rho_e} + \Delta t\boldsymbol{C}_{\rho_e} + 0.5\Delta t^2\partial_t(\boldsymbol{C}_{\rho_e}),\end{aligned} \tag{20}$$

where $\mathbf{m}_g = \mathbf{M}g_n$ is associated with the incompressible Navier–Stokes equations, and $\mathbf{m}_{\rho_e} = \mathbf{M}f_{\rho_e}$ corresponds to the charge conservation equation. After the collision step in raw moment space, the distribution functions are reconstructed as $g_i = \mathbf{M}^{-1}\mathbf{m}_g^*$ and $f_{\rho_e} = \mathbf{M}^{-1}\mathbf{m}_{\rho_e}^*$. For the Poisson equation, an inner iteration is required at each time step to reach the steady state. To reduce the computational cost, a D3Q7 single-relaxation-time collision operator is adopted to solve the Poisson equation:

$$f_{\psi,i}^* = f_{\psi,i} - \frac{1}{\tau_\psi}\left(f_{\psi,i} - f_{\psi,i}^{eq}\right) + \Delta t' C_{\psi,i} + 0.5\Delta t'^2\partial_t(C_{\psi,i}), \tag{21}$$

where $\Delta t' = 1$ is the inner iteration time step. In the above equations, the discrete equilibrium moment sets and the discrete forcing terms, including $\mathbf{m}_{\rho_e}^{\mathrm{eq}}$, $\mathbf{m}_g^{\mathrm{eq}}$, $\mathbf{R}_g$, $\mathbf{R}_{\rho_e}$, $\mathbf{C}_{\rho_e}$, $f_{\psi,i}^{\mathrm{eq}}$ and $\mathbf{C}_{\psi,i}$, are given explicitly in our previous work studies [22,43] According to the Chapman–Enskog analysis in our recent studies [22,49], it has been demonstrated that the above LBM model can accurately reproduce the incompressible NS equations, the charge conservation equation, and the Poisson equation. The detailed derivations are not repeated here for brevity.

Model validations

In this work, the proposed model is comprehensively validated by comparing our simulations with available experimental and simulation studies. It should be noted that the EHD multiphase model employed here has been extensively validated in our recent studies [22,43]. Therefore, we focus on validating the additional ternary multiphase model in this section. Firstly, we reproduce the experiments of Planchette et al. [50], in which a glycerol-solution droplet and a silicone-oil droplet with the same initial diameter D_0 undergo head-on collisions with different relative velocities V_0 and off-centre distances X.

We simulate two cases with different impact parameters (i.e., (a) $D_0 = 230$ μm, $V_0 = 2.30$ m/s, $X = 0.03$ and (b) $D_0 = 190$ μm, $V_0 = 2.75$ m/s, $X = 0.49$). As shown in Fig. 6, the numerical results agree well with the experimental observations [50]. In particular, for the higher impact velocity case, the simulations successfully capture the “cross-separation”

mechanism reported experimentally, where only a pure droplet of the encapsulating liquid remains after collision, together with the formation of satellite droplets.

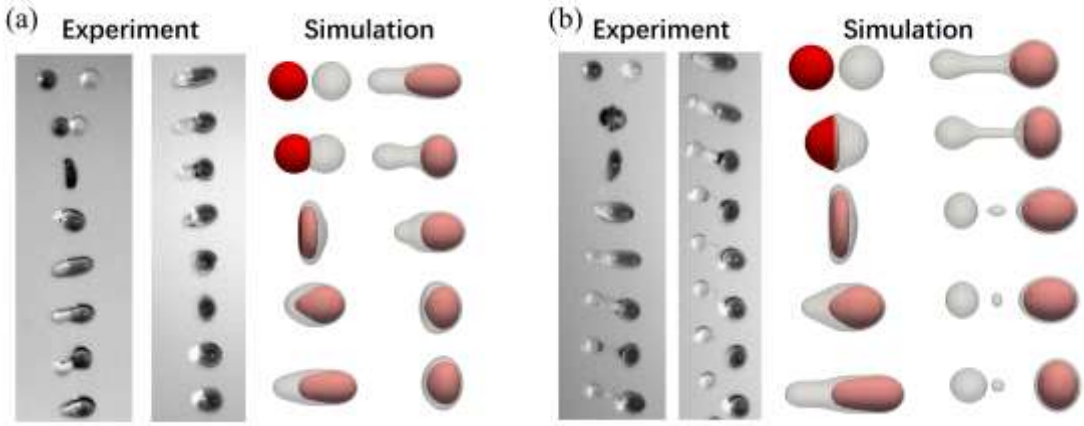


Figure 6. A qualitative comparison between experimental and numerical results for head-on collisions of a glycerol-solution droplet and a silicone-oil droplet.

Next, we validate the translational mobility of droplets on LIS, following previous experimental [33] and numerical studies [23]. We reproduce droplet sliding on LIS driven by a fixed body force ($F_{\mathrm{x}} = mg_x$), using the similar configuration ($\phi = 0.25$, Bond number $\mathrm{Bo} = R_0^2 g_x/\gamma_{\mathrm{wg}} = 0.112$ and apparent angle $\theta_{\mathrm{app}} = 90°$) to experiment in Ref. [33]. In this case, the lubricant viscosity is set to $\mu_{\mathrm{o}} = 10\mu_{\mathrm{ref}}$, where $\mu_{\mathrm{ref}} = 1\mathrm{cP}$ is the reference viscosity. The droplet viscosity is varied over the range $\mu_{\mathrm{w}} = 1 \sim 500$ cP. Similar to Ref. [23], we scale the droplet terminal velocity V_{t} by V_{ref}, where V_{ref} is defined as the terminal sliding velocity for the case with $\mu_w = \mu_{\mathrm{ref}}$.

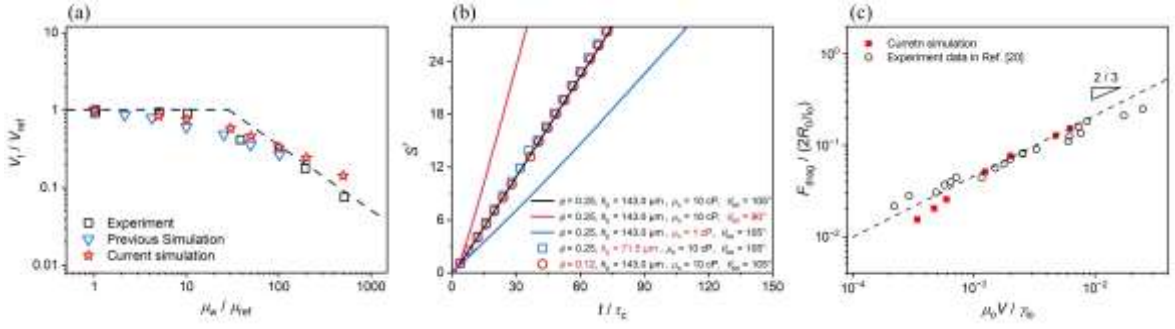


Figure 7. Simulation of droplet sliding on LIS driven by a constant body force: (a) comparison of our simulation results with experimental data [33] and previous numerical results [34] for the droplet terminal velocity V_t; (b) parameter sensitivity analysis with respect to μ_o, θ_{ws}, ϕ, and h_p.(c) The normalized drag force $F_{\mathrm{drag}}/(2\gamma_{ow}R_0)$ as a function of $\mu_o V/\gamma_{lo}$ during droplet motion in the lubrication dissipation regime, where the red symbols and dashed line denote the experimental data and theoretical equation in Ref. [20].

As shown in Fig. 7(a), for high-viscosity droplets, viscous dissipation occurs predominantly within the droplet. In this regime, the terminal velocity decreases with

increasing droplet viscosity, following $V_t \propto \mu_w^{-1}$, and eventually approaches $V_t \approx V_{\mathrm{ref}}$. In both simulations [34] and experiment [33], this transition occurs at approximately $\mu_w \sim 2\mu_o$. Besides, we extend the case with $\mu_w = \mu_o$ in Fig. 7(b) to different μ_o, θ_{ws}, ϕ, and h_p to assess parameter sensitivity. The results show that variations in μ_o and θ_{ws} have a dominant effect on droplet translational mobility. By contrast, the geometric parameters have little influence, even when ϕ and h_p are reduced by half. This observation is consistent with the previous numerical findings [34].

In addition to the droplet dissipation dominated regime as discussed above, we also performed simulations to validate F_{drag} in the lubrication dissipation regime. In this case, we set $R_0 = 0.5\,\mathrm{mm}$, $\mu_o = 100\,\mathrm{cP}$, $\theta_{ws} = 105^\circ$, and $\theta_{os} = 5^\circ$. The droplet was driven by a constant horizontal force ranging from $0.6\mathrm{mg}$ to $6\mathrm{mg}$, and was allowed to accelerate until reaching a steady state. Figure 7(c) presents the quantitative relationship between F_{drag}, and Ca. Our simulations successfully reproduce the $F_{\mathrm{drag}} \sim \mathrm{Ca}^{2/3}$ scaling law and agree well with the experimental results reported in the Ref. [20]. These results further demonstrate that the present numerical method can accurately capture droplet drag over a broad range of lubricant viscosities.

Data and code availability

The data and code generated in this study are available from the lead contact upon reasonable request.

Acknowledgements

Support from National Natural Science Foundation of China (No. 12502317), National Key R&D Program of China (Grant No. 2022YFF0503501), the UK Engineering and Physical Sciences Research Council under the project “UK Consortium on Mesoscale Engineering Sciences (UKCOMES)” (Grant No. EP/X035875/1) and “Multiphase Multicomponent Lattice Boltzmann Method for Modelling Wetting on Liquid Infused Surfaces” (Grant No. EP/V034154/2), Leverhulme Trust (Research Project RPG-2022-140) are gratefully acknowledged.

Bibliography

[1] S. P. Zhang et al., *Digital Acoustofluidics Enables Contactless and Programmable Liquid Handling*, Nat. Commun. **9**, 1 (2018).

[2] M. Abdelgawad and A. R. Wheeler, *The Digital Revolution: A New Paradigm for Microfluidics*, Adv. Mater. **21**, 920 (2009).

[3] D. Wu et al., *High-Performance Unidirectional Manipulation of Microdroplets by Horizontal Vibration on Femtosecond Laser-Induced Slant Microwall Arrays*, Adv. Mater. **32**, 1 (2020).
[4] J. Sun, Q. Zhao, Z. Mo, J. Chen, H. Guo, and L. Zhang, *Self-Powered Droplet Manipulation for Full Human-Droplet Interaction in Multiple Mediums*, Nat. Commun. **16**, 1 (2025).
[5] J. Wang, T. Lu, M. Yang, D. Sun, Y. Xia, and T. Wang, *Hydrogel 3D Printing with the Capacitor Edge Effect*, Sci. Adv. **5**, 1 (2019).
[6] Y. Zheng, H. Bai, Z. Huang, X. Tian, F. Q. Nie, Y. Zhao, J. Zhai, and L. Jiang, *Directional Water Collection on Wetted Spider Silk*, Nature **463**, 640 (2010).
[7] S. Zhang, J. Huang, Z. Chen, and Y. Lai, *Bioinspired Special Wettability Surfaces: From Fundamental Research to Water Harvesting Applications*, Small **13**, 1 (2017).
[8] L. Wu, Z. Guo, and W. Liu, *Surface Behaviors of Droplet Manipulation in Microfluidics Devices*, Adv. Colloid Interface Sci. **308**, 102770 (2022).
[9] J. Xu, S. Xiu, Z. Lian, H. Yu, and J. Cao, *Bioinspired Materials for Droplet Manipulation: Principles, Methods and Applications*, Droplet **1**, 11 (2022).
[10] F. Wang, M. Liu, C. Liu, Q. Zhao, T. Wang, Z. Wang, and X. Du, *Light-Induced Charged Slippery Surfaces*, Sci. Adv. **8**, 1 (2022).
[11] Z. Yuan, C. Lu, C. Liu, X. Bai, L. Zhao, S. Feng, and Y. Liu, *Ultrasonic Tweezer for Multifunctional Droplet Manipulation*, Sci. Adv. **9**, 1 (2023).
[12] Y. Jin, C. Wu, P. Sun, M. Wang, M. Cui, C. Zhang, and Z. Wang, *Electrification of Water: From Basics to Applications*, Droplet **1**, 92 (2022).
[13] M. K. Chaudhury et al., *On-Chip Manipulation of Free Droplets Tiny Free-Floating Drops Can Be Driven across a Liquid Medium by an Electric Field*, Curr. Opin. Coll. Interface Sci **256**, 2240 (1992).
[14] H. Dai, C. Gao, J. Sun, C. Li, N. Li, L. Wu, Z. Dong, and L. Jiang, *Controllable High-Speed Electrostatic Manipulation of Water Droplets on a Superhydrophobic Surface*, Adv. Mater. **31**, 1 (2019).
[15] Y. Jin, W. Xu, H. Zhang, R. Li, J. Sun, S. Yang, M. Liu, H. Mao, and Z. Wang, *Electrostatic Tweezer for Droplet Manipulation*, Proc. Natl. Acad. Sci. U. S. A. **119**, (2022).
[16] J. Yong, X. Li, Y. Hu, Y. Wang, Y. Peng, Z. Chen, Y. Zhang, S. Zhu, C. Wang, and D. Wu, *Portable Triboelectric Electrostatic Tweezer for External Manipulation of Droplets within a Closed Femtosecond Laser-Treated Superhydrophobic System*, Nano Lett. **24**, 7116 (2024).
[17] J. Yong, X. Li, Y. Hu, Y. Peng, Z. Cheng, T. Xu, C. Wang, and D. Wu, *Triboelectric 'Electrostatic Tweezers' for Manipulating Droplets on Lubricated Slippery Surfaces Prepared by Femtosecond Laser Processing*, Int. J. Extrem. Manuf. **6**, (2024).
[18] J. Hartmann, M. T. Schür, and S. Hardt, *Manipulation and Control of Droplets on Surfaces in a Homogeneous Electric Field*, Nat. Commun. **13**, (2022).
[19] S. Hardt and G. McHale, *Flow and Drop Transport Along Liquid-Infused Surfaces*, Annu. Rev. Fluid Mech. **54**, 83 (2021).
[20] M. J. Kreder, D. Daniel, A. Tetreault, Z. Cao, B. Lemaire, J. V. I. Timonen, and J. Aizenberg, *Film Dynamics and Lubricant Depletion by Droplets Moving on Lubricated Surfaces*, Phys. Rev. X **8**, 31053 (2018).
[21] Z. Chen, X. Li, C. Wang, C. Chen, S. Zhu, Y. Hu, J. Yong, and D. Wu, *A Digital Microfluidic Droplet Robotic System Enabled by Programmed Electrostatic Tweezer Arrays and Femtosecond Laser-Engineered Insulating Superhydrophobic Platforms*, Nano Lett. (2025).

[22] G. Wang, T. Lei, J. Yang, L. Fei, J. Chen, and K. H. Luo, *Lattice Boltzmann Modelling and Study of Droplet Equatorial Streaming in an Electric Field*, J. Fluid Mech. **988**, 1 (2024).
[23] M. S. Sadullah, C. Semprebon, and H. Kusumaatmaja, *Drop Dynamics on Liquid-Infused Surfaces: The Role of the Lubricant Ridge*, Langmuir **34**, 8112 (2018).
[24] M. S. Sadullah, G. Launay, J. Parle, R. Ledesma-Aguilar, Y. Gizaw, G. McHale, G. G. Wells, and H. Kusumaatmaja, *Bidirectional Motion of Droplets on Gradient Liquid Infused Surfaces*, Commun. Phys. **3**, 1 (2020).
[25] F. Schellenberger, J. Xie, N. Encinas, A. Hardy, M. Klapper, P. Papadopoulos, H. J. Butt, and D. Vollmer, *Direct Observation of Drops on Slippery Lubricant-Infused Surfaces*, Soft Matter **11**, 7617 (2015).
[26] J. D. Smith, R. Dhiman, S. Anand, E. Reza-Garduno, R. E. Cohen, G. H. McKinley, and K. K. Varanasi, *Droplet Mobility on Lubricant-Impregnated Surfaces*, Soft Matter **9**, 1772 (2013).
[27] A. Lafuma and D. Quéré, *Slippery Pre-Suffused Surfaces*, EPL **96**, 1 (2011).
[28] A. Naga, L. R. J. Scarratt, C. Neto, P. Papadopoulos, and D. Vollmer, *Drop Friction and Failure on Superhydrophobic and Slippery Surfaces*, ACS Nano **19**, 18902 (2025).
[29] A. Keiser, P. Baumli, D. Vollmer, and D. Quéré, *Universality of Friction Laws on Liquid-Infused Materials*, Phys. Rev. Fluids **5**, 1 (2020).
[30] D. Daniel, J. V. I. Timonen, R. Li, S. J. Velling, M. J. Kreder, A. Tetreault, and J. Aizenberg, *Origins of Extreme Liquid Repellency on Structured, Flat, and Lubricated Hydrophobic Surfaces*, Phys. Rev. Lett. **120**, 244503 (2018).
[31] D. Daniel, J. V. I. Timonen, R. Li, S. J. Velling, and J. Aizenberg, *Oleoplaning Droplets on Lubricated Surfaces*, Nat. Phys. **13**, 1020 (2017).
[32] P.-G. De Gennes, F. Brochard-Wyart, and D. Quéré, *Capillarity and Wetting Phenomena: Drops, Bubbles, Pearls, Waves* (Springer Science \& Business Media, 2003).
[33] A. Keiser, L. Keiser, C. Clanet, and D. Quéré, *Drop Friction on Liquid-Infused Materials*, Soft Matter **13**, 6981 (2017).
[34] A. Naga, M. Rennick, L. Hauer, W. S. Y. Wong, A. Sharifi-Aghili, D. Vollmer, and H. Kusumaatmaja, *Direct Visualization of Viscous Dissipation and Wetting Ridge Geometry on Lubricant-Infused Surfaces*, Commun. Phys. **7**, 306 (2024).
[35] A. K. Srivastava, M. Kim, S. M. Kim, M. K. Kim, K. Lee, Y. H. Lee, M. H. Lee, and S. H. Lee, *Dielectrophoretic and Electrophoretic Force Analysis of Colloidal Fullerenes in a Nematic Liquid-Crystal Medium*, Phys. Rev. E - Stat. Nonlinear, Soft Matter Phys. **80**, 1 (2009).
[36] C. Sorgentone and P. M. Vlahovska, *Tandem Droplet Locomotion in a Uniform Electric Field*, J. Fluid Mech. **951**, 1 (2022).
[37] G. I. Taylor, A. D. McEwan, and L. N. J. de Jong, *Studies in Electrohydrodynamics. I. The Circulation Produced in a Drop by an Electric Field*, Proc. R. Soc. London. Ser. A. Math. Phys. Sci. **291**, 159 (1966).
[38] R. Haghani Hassan Abadi, M. H. Rahimian, and A. Fakhari, *Conservative Phase-Field Lattice-Boltzmann Model for Ternary Fluids*, J. Comput. Phys. **374**, 668 (2018).
[39] S. O. Unverdi and G. Tryggvason, *A Front-Tracking Method for Viscous, Incompressible, Multi-Fluid Flows*, J. Comput. Phys. **100**, 25 (1992).
[40] H. Liang, B. C. Shi, and Z. H. Chai, *Lattice Boltzmann Modeling of Three-Phase Incompressible Flows*, Phys. Rev. E **93**, 1 (2016).
[41] J. R. Melcher and G. I. Taylor, *Electrohydrodynamics: A Review of the Role of Interfacial Shear Stresses*, Annu. Rev. Fluid Mech. **1**, 111 (1969).

[42] P. M. Vlahovska, *Electrohydrodynamics of Drops and Vesicles*, Annu. Rev. Fluid Mech. **51**, 305 (2019).
[43] G. Wang, J. Yang, T. Lei, L. Fei, X. Zhao, J. Zhao, K. Li, and K. H. Luo, *Mesoscopic Insights into Effects of Electric Field on Pool Boiling for Leaky Dielectric Fluids*, Commun. Phys. **8**, (2025).
[44] K. H. Luo, L. Fei, and G. Wang, *A Unified Lattice Boltzmann Model and Application to Multiphase Flows*, Philos. Trans. R. Soc. A Math. Phys. Eng. Sci. **379**, 20200397 (2021).
[45] L. Fei, K. H. Luo, and Q. Li, *Three-Dimensional Cascaded Lattice Boltzmann Method: Improved Implementation and Consistent Forcing Scheme*, Phys. Rev. E **97**, 053309 (2018).
[46] L. Fei, J. Du, K. H. Luo, S. Succi, M. Lauricella, A. Montessori, and Q. Wang, *Modeling Realistic Multiphase Flows Using a Non-Orthogonal Multiple-Relaxation-Time Lattice Boltzmann Method*, Phys. Fluids **31**, (2019).
[47] F. Ren, B. Song, M. C. Sukop, and H. Hu, *Improved Lattice Boltzmann Modeling of Binary Flow Based on the Conservative Allen-Cahn Equation*, Phys. Rev. E **94**, 1 (2016).
[48] A. Zarareh, S. Khajepor, S. B. Burnside, and B. Chen, *Improving the Staircase Approximation for Wettability Implementation of Phase-Field Model: Part 1 – Static Contact Angle*, Comput. Math. with Appl. **98**, 218 (2021).
[49] G. Wang, J. Yang, T. Lei, J. Chen, Q. Wang, and K. H. Luo, *A Three-Dimensional Non-Orthogonal Multiple-Relaxation-Time Phase-Field Lattice Boltzmann Model for Multiphase Flows at Large Density Ratios and High Reynolds Numbers*, Int. J. Multiph. Flow **168**, 104582 (2023).
[50] C. Planchette, E. Lorenceau, and G. Brenn, *Liquid Encapsulation by Binary Collisions of Immiscible Liquid Drops*, Colloids Surfaces A Physicochem. Eng. Asp. **365**, 89 (2010).

Supplementary Files

This is a list of supplementary files associated with this preprint. Click to download.

- SupplementaryMovie1.gif
- SupplementaryMovie2.gif
- Supplementarymaterial.docx